Numerical simulation and experimental validation of a multi-step deep drawing process

Matías Pacheco, Diego Celentano, Claudio García-Herrera, Julio Méndez & Fernando Flores

EDITOR-IN-CHIEF : *Francisco Chinesta*

International Journal of
Material Forming

ISSN 1960-6206
Volume 10 - Number 1
January 2017

Official Journal of the European Scientific Association for Material Forming – ESAFORM

Thematic Issue: Computational Methods in Manufacturing

Editorial for thematic issues: computational methods in manufacturing
J.-P. Ponthot, E. Feulvarch, S. Drapier, J.-M. Bergheau

A stabilized P1/P1 finite element for the mechanical analysis of solid metals
E. Feulvarch, H.A. El Sayed, J.-C. Roux, J.-M. Bergheau

Numerical simulation and experimental validation of a multi-step deep drawing process
M. Pacheco, D. Celentano, C. García-Herrera, J. Méndez, F. Flores

Investigation of the effect of temper rolling on the texture evolution and mechanical behavior
of IF steels using multiscale simulation
K. Soho, X. Lemoine, F. Abed-Meraim, H. Zahrouni

Resin infusion-based processes simulation : coupled Stokes-Darcy flows in orthotropic preforms
undergoing finite strain
M. Blais, N. Moulin, P.-J. Liotier, S. Drapier

On the numerical simulation of sheet metal blanking process
C. Canales, P. Bussetta, J.-P. Ponthot

Finite element analysis of combined forming processes by means of rate dependent ductile
damage modelling
Y. Kiliclar, I.N. Vladimirov, S. Wulfinghoff, S. Reese, O.K. Demir, C. Weddeling, A.E. Tekkaya,
M. Engelhardt, C. Klose, H.J. Maier, M. Rozgić , M. Stiemer

Original Research

Comparison of different yield criteria in various deep drawn cups
F. Cogun, H. Darendeliler

The stribeck curve in cold flat rolling
M. Szucs, G. Krallics, J.G. Lenard

Influence of plastic deformation in flexible pad laser shock forming – experimental
and numerical analysis
B. Nagarajan, S. Castagne, Z. Wang, H.Y. Zheng, K. Nadarajan

Numerical and experimental analysis of wrinkling during the cup drawing of an AA5042
aluminium alloy
D.M. Neto, M.C. Oliveira, R.E. Dick, P.D. Barros, J.L. Alves, L.F. Menezes

Springer

>springer.com

Springer

Springer

CrossMark

THEMATIC ISSUE: COMPUTATIONAL METHODS IN MANUFACTURING

Numerical simulation and experimental validation of a multi-step deep drawing process

Matías Pacheco[1] · Diego Celentano[2] · Claudio García-Herrera[1] · Julio Méndez[1] · Fernando Flores[3]

Abstract This paper presents the numerical simulation of an industrial multi-step deep drawing process. A large strain finite element formulation including a hyperelastic elastoplastic constitutive model and a contact-friction law is used to this end where the steel sheet material parameters considered in the analysis are previously derived through a characterization procedure of its mechanical response. The numerical predictions of the final shape and thickness distribution of the blank are compared and discussed with available experimental values measured at the end of three successive drawing steps. In addition, a plastic work-based damage index is used to assess failure occurrence during the process. The damage values computed at the end of the drawing process are found to be lower than that corresponding to rupture in the tensile test, considered here as the threshold of failure, confirming, as observed experimentally, that neither fracture nor necking is developed in the blank during the whole drawing process. Finally, the possibility to carry out a reduced two-step drawing process, obtained by merging the second and third steps of the three-step process, is precluded since the damage criterion predicts in this case excessively large values that indicate that failure may occur in specific zones of the sheet.

Keywords Multi-step deep drawing · Simulation of industrial problems · Material characterization · Damage estimation

✉ Diego Celentano
  dcelentano@ing.puc.cl

  Matías Pacheco
  matias.pacheco@usach.cl

  Claudio García-Herrera
  claudio.garcia@usach.cl

  Julio Méndez
  julio.mendezop@usach.cl

  Fernando Flores
  fflores@efn.uncor.edu

[1] Departamento de Ingeniería Mecánica, Universidad de Santiago de Chile (USACH), Av. Bernardo O'Higgins, 3363 Santiago de Chile, Chile

[2] Departamento de Ingeniería Mecánica y Metalúrgica, Pontificia Universidad Católica de Chile, Av. Vicuña Mackenna, 4860 Santiago de Chile, Chile

[3] Departamento de Estructuras, Universidad Nacional de Córdoba, Casilla de Correo 916, 5000 Córdoba, Argentina

Introduction

There exist nowadays many products that are manufactured by sheet metal forming. Specifically, those obtained via the deep drawing process play an important role in the automotive and food industries, among others. One of the most relevant aspects involved in the analysis of this kind of problem is the need to achieve an adequate knowledge of the mechanical behaviour of the sheet material since complex phenomena (e.g., finite strain plasticity, hardening effects, damage, texture development, defect formation, etc.) take place during its deformation. Other important features of the process are the correct estimations of both the contact conditions between the blank and the different tools and, in multi-step drawing operations, the stresses and strains that develop in previous stages.

A great variety of models have been proposed during the last decades to describe the material behavior during sheet

⚡ Springer

forming (see e.g. [1] for a recent review on this subject). However, the anisotropic Hill-48 criterion [2] is still nowadays, due its prediction capabilities and simplicity, one of the most widely used models to this end [3]. In recent years, this model has been successfully applied to the numerical simulation of industrial deep drawing processes [4]. Moreover, the stress–strain paths computed in this context are the basis of several ductile damage criteria aimed at estimating the occurrence of failure of the blank [5–7]. Although the final aim of these analyses is the further control and/or optimization of the process, a procedure that needs to be carried out in advance is the full experimental validation of the results provided by the simulation. This is usually a hard task owing to the inherent difficulties associated with the measurements of the different variables present in the problem.

This paper presents the modeling and the corresponding experimental validation of an industrial multi-step sheet metal forming process consisting in the deep drawing of a steel clutch lid of a commercial washing machine. The soundness of this component at the end of its forming is crucial due to the dynamic nature of the loads that will act on it during its service life. The galvanized steel used for this component is commercially known as A-G90. Firstly, the characterization of the mechanical behavior of this material is carried out by means of the tensile test conducted according to the standard specifications. The experimentally derived elastic and plastic parameters are the basic data for the constitutive model adopted to describe the material response during its deformation. To this end, a hyperelastic elastoplastic law written in terms of Hencky stress and strain measures under the plane stress condition is considered. Hollomon-type hardening and normal anisotropy (along the sheet thickness) effects are both accounted for through the Hill-48 associate yield function. In addition, a plastic work-based damage index is also considered where the value corresponding to rupture in the tensile test is adopted here as the threshold of failure. The material constitutive model and characterization are respectively presented in "Material constitutive model" and "Material characterization sections". Afterwards, this model is considered for the simulation of the above mentioned industrial application. A large strain shell formulation discretized within the context of the finite element method via thin three-noded triangles with only translational degrees of freedom is used for this purpose [8]. The mechanical interactions between the sheet and the different tools (punch, blankholder and die) are taken into account through a Coulomb-type contact-friction law. Although the good performance of this formulation has been extensively checked in different well-known benchmark problems [8–10] and,

more recently, it has been experimentally validated in laboratory tests and single-step industrial applications [4], the main objective of this work is to assess and validate its numerical response in the analysis of a more complex industrial application such as the present multi-steep deep drawing process. The results obtained in this study are described and discussed in "Industrial application" section.

Table 1　Material constitutive model: basic equations and nomenclature

Basic equations

- Hyperelastic stress–strain law: $\mathbf{T}=\mathbf{C}:(\mathbf{e}-\mathbf{e}^p)$ (plane stress condition is assumed)
- Hencky deformation tensor: $\mathbf{e}=\mathbf{L}^T \ln(\mathbf{\Lambda})\mathbf{L}$
- Evolution of the plastic contribution of $\mathbf{e}$: $\dot{\mathbf{e}}^p = \dot{\lambda}\frac{\partial F}{\partial \boldsymbol{\sigma}}$ (associate plasticity is considered)
- Anisotropic Hill-48 yield function: $\overline{\sigma} = \sigma_{11}^2 + \sigma_{22}^2 - \frac{2\overline{R}}{1+\overline{R}}\sigma_{11}\sigma_{22} + \frac{2(1+2\overline{R})}{1+\overline{R}}\sigma_{12}^2$
- Isotropic strain hardening (Hollomon-type) function: $C^p = A^p \left(\overline{e}_0^p + \overline{e}^p\right)^{n^p}$
- Damage criterion: $D = \int_0^{\overline{e}^p} \overline{\sigma}\, d\overline{e}^p \leq D^f = \int_0^{\overline{e}^f} \overline{\sigma}\, d\overline{e}^p$

Nomenclature

- $\mathbf{F}$: deformation gradient tensor
- $\mathbf{U}$: right stretch tensor $\mathbf{U}$ ($\mathbf{U}^2 = \mathbf{F}^T \mathbf{F}$)
- $\mathbf{\Lambda}=[\lambda_\alpha]$, $\mathbf{L}$: eigenvalues and eigenvectors of $\mathbf{U}$, respectively (α=1,2,3)
- ^{T}: transpose symbol
- $\mathbf{T}$: Hencky stress tensor
- $\mathbf{C}$: plane stress isotropic elastic constitutive tensor
- $\dot{\lambda}$: increment of the plastic consistency parameter (computed, as usual, from the consistency condition $\dot{F} = 0$)
- $\boldsymbol{\sigma}$: Cauchy stress tensor; $\boldsymbol{\sigma}$ is computed from $\mathbf{T}$ according to the following transformations:
   1) $\mathbf{T}_L = \mathbf{L}^T \mathbf{T}\, \mathbf{L}$ (rotated $\mathbf{T}$)
   2) $[\mathbf{S}_L]_{\alpha\alpha} = \frac{1}{\lambda_\alpha^2}[\mathbf{T}_L]_{\alpha\alpha}$ and $[\mathbf{S}_L]_{\alpha\beta} = \frac{2\ln(\lambda_\alpha/\lambda_\beta)}{(\lambda_\alpha^2-\lambda_\beta^2)}[\mathbf{S}_L]_{\alpha\beta}$ (rotated $\mathbf{S}$)
   3) $\mathbf{S} = \mathbf{L}\mathbf{S}_L\mathbf{L}^T$ (Second Piola-Kirchhoff stress)
   4) $\boldsymbol{\sigma} = \frac{1}{\det(\mathbf{F})}\mathbf{F}\,\mathbf{S}\,\mathbf{F}^T$
- $\overline{\sigma}$: Equivalent von Mises stress $\left(F = \sigma_{11}^2 + \sigma_{22}^2 - \frac{2\overline{R}}{1+\overline{R}}\sigma_{11}\sigma_{22} + \frac{2(1+2\overline{R})}{1+\overline{R}}\sigma_{12}^2 - (C^p)^2 = 0\right)$
- $\overline{R}$: average Lankford's coefficient
- A^p, n^p: hardening parameters
- $\overline{e}^p$: effective plastic deformation (its rate is computed as $\dot{\overline{e}}^p = \sqrt{2/3\dot{\mathbf{e}}^p : \dot{\mathbf{e}}^p}$)
- $\overline{e}_0^p$: assumed initial value of $\overline{e}^p$ such that $\sigma_y = A^p\left(\overline{e}_0^p\right)^{n^p}$
- σ_y: yield strength (it defines the initial elastic domain)
- D: damage index with D^f being its threshold of failure
- $\overline{e}^f$: effective plastic deformation at rupture in the tensile test
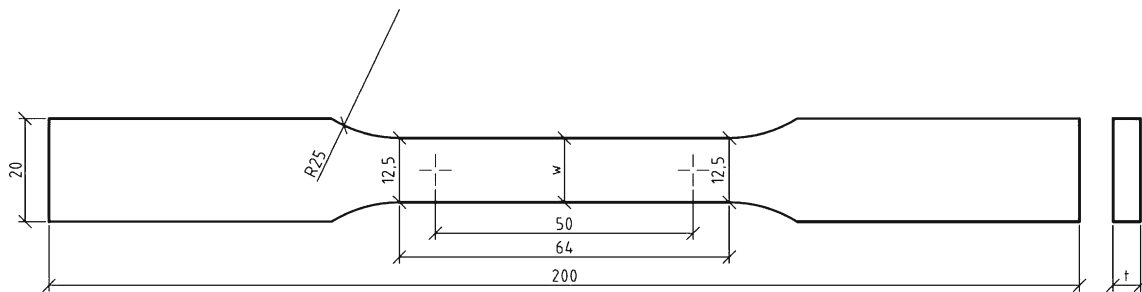
Fig. 1 Tensile specimen (dimensions in mm)

The experimental validation is focused on the thickness and damage profiles along two representative lines of the sheet attained at the end of three successive drawing steps. The damage values computed at the end of the drawing process confirm the experimental observation that neither fracture nor necking is developed in the blank during the whole drawing process. Moreover, the damage criterion is used to discard the possibility to reduce the number of drawing steps needed to achieve the same final deformed part since excessively large damage values are predicted in specific zones of the sheet. Finally, the conclusions are presented in "Conclusions" section.

Material constitutive model

An associate elastoplastic constitutive model under the plane stress condition is adopted in this work to describe the sheet material behavior. As usual, the sheet is considered as a thin shell with a curvilinear local coordinate system over its middle surface at which the stress and strains are referred to. Table 1 summarizes the basic equations of this model [8]: the hyperelastic stress–strain law, the evolution of the plastic deformation, the anisotropic yield criterion, the isotropic hardening function and the damage criterion.

It is seen that the so-called Hencky deformation tensor is chosen here as the main kinematic state variable since it is an objective (Lagrangian) strain measure and constitutes, in addition, a natural extension of the unidimensional logarithmic strain. Note that the strain related to the sheet thickness variation is simply $e_3 = \ln(t/t_0)$, where t/t_0 is the thickness ratio between the deformed and initial configurations. This ratio is computed assuming an isochoric behavior disregarding the expansion/contraction due to the Poisson effect. The other two eigenvalues of **U** define the principal (in-plane) stretches in the shell surface. In this context, an additive elastic–plastic decomposition of the Hencky strain is assumed based on the fact that the elastic strains are usually small in comparison with plastic strains in most steel deep drawing processes.

Fig. 2 Tensile test: average engineering stress–strain curves of A-G90 steel for specimens oriented at 0, 45 and 90° with respect to the rolling direction

Fig. 3 Geometric configuration of the broken tensile sample

Table 2 Average original and final dimensions of the A-G90 steel tensile samples

	Original	Final 0°	Final 45°	Final 90°	Final mean	Ratio (Final Mean/Original)
Extensometer length (mm)	50.00	75.71	74.36	74.36	74.81	1.50
Thickness (mm)	1.50	0.96	0.88	0.96	0.93	0.62
Width (mm)	12.50	7.45	7.85	7.43	7.58	0.61
Transversal area (mm^2)	18.75	7.18	6.68	7.15	7.07	0.38

Moreover, as already mentioned, it has been long recognized that the use of the associate rate independent plasticity theory including the classical anisotropic Hill-48 yield criterion is a useful framework to simulate sheet responses subjected to deep drawing operations. Although the further assumption of planar isotropy (or normal anisotropy) appreciably simplifies the formulation, this situation was found to be approximately fulfilled in many sheet forming applications. In this context, the yield function is written in terms of the Cauchy stress tensor σ. The elastic–plastic constitutive equations are integrated resorting to a backward-Euler predictor-corrector scheme that normally converges in 1 or 2 iterations due to the small time steps used in the analysis. The condition $\sigma_{33} = 0$ is satisfied directly by the plane-stress elastic constitutive relation between the elastic components of the logarithmic strain and the Kirchhoff stresses. The transformations that allow the computation of σ from the Hencky stress tensor **T** are also detailed in Table 1. More details about this model can be found in [8].

In addition, a plastic work-based damage criterion extensively used in different forming processes [11] is adopted in the present analysis to evaluate the possibility of fracture development during the whole deformation stages of the blank.

As described below, the yield strength σ_y, together with the hardening parameters A^P and n^P, the average Lankford's coefficient $\overline{R}$ and the damage threshold of failure D^f are all obtained from experimental data measured during tensile testing.

Material characterization

Tensile test

An experimental procedure aimed at characterizing the mechanical behaviour of the A-G90 steel, which is the drawing material used in the industrial application to be described in "Industrial application" section, is firstly performed through the tensile test. This electro-galvanized steel has appropriate mechanical and surface properties that make it extremely suitable for metal forming applications: wide range of formability, same weldability as hot/cold rolled material, excellent paintability, good corrosion resistance, anti-fingerprint and surface conductivity [12].

The tensile test is carried out in this work according to the standard specifications [13, 14]. Figure 1 shows the sample geometric configuration employed for the tests. The distance between the two markers denotes the initial extensometer length taken as 50 mm in this case. The respective initial values for the width and thickness in the working zone are $w_0 = 12.5$ mm and $t_0 = 1.5$ mm. The specimens have been cut along three different orientations (0, 45 and 90°) with respect to the rolling direction of the sheet during its manufacturing process. A nearly gradual reduction in width is considered in order to trigger the necking development that has to take place approximately at the middle of the extensometer length. This tapered profile fits the usual standards since the difference between the adopted maximum and minimum width values existing in the extensometer length is lower than 1 %.

Table 3 Parameters obtained from the tensile test applied to A-G90 steel samples

	0°	45°	90°	Average	Range (±)
Young's modulus (MPa)	136.19	158.58	147.32	147.36	14.90
Yield strength (MPa)	162.26	172.88	168.38	167.84	5.10
Maximum load (kN)	5.33	5.47	5.23	5.34	0.11
Maximum strength (MPa)	284.07	291.55	279.01	284.88	5.80

Considering a load cell speed of 2.5 mm/min, 15 samples (5 for each orientation) were tested. The average engineering stress–strain curves associated with the three orientations are plotted in Fig. 2. The uniformity of the material is reflected in the remarkable low dispersion found in the measurements for each orientation. As usual, the engineering stress is defined as P/A_0, where P is the axial load and A_0 is the initial transversal area defined as $A_0 = w_0 t_0$. The engineering strain or elongation is defined as $(L - L_0)/L_0$ with L and L_0 being the current and initial extensometer lengths, respectively. At the beginning of the deformation process, the material behaves elastically. Once the yield strength is reached, plastic hardening takes place and the load increases up to a maximum value that holds approximately constant within a large elongation interval (20 to 34 %). As it is well known, the load decreases for higher levels of deformation since the effect of the reduction of the transversal area at the necking zone is stronger than that of the hardening mechanism. The geometric configuration of the broken sample shown in Fig. 3 exhibits a highly localized (ductile) necking. Table 2 summarizes the average original and final dimensions of the samples while some parameters obtained from the test measurements are presented in Table 3.

Hardening parameters

According to [15], the derivation of the hardening parameters A^P and n^P involves the consideration of an alternative stress–strain relationship written in terms of an equivalent stress $\sigma_{eq} = f_B P/A$ and an equivalent strain $\varepsilon_{eq} = \sigma_{eq}/E + \varepsilon_P$, where $f_B(\varepsilon_P) \leq 1$ is an assumed known correction
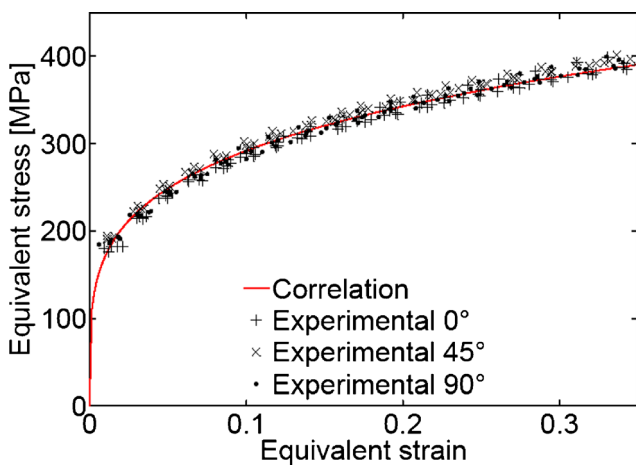
Table 4 Lankford's coefficients and earing index of A-G90 galvanized steel

	R_0	R_{45}	R_{90}	$\overline{R}$	ΔR
Average	2.05	1.56	2.27	1.86	0.60
Range (±)	0.19	0.03	0.22	–	–

factor [16] applied to the mean true axial stress P/A, A is the current transversal area at the necking zone ($A = wt$, where w and t are the current width and thickness, respectively), E is the Young's modulus and $\varepsilon_P = \ln(A_0/A)$ is the true (logarithmic) deformation. As can be seen, w and t are the additional variables to be measured. It should be mentioned that prior to the onset of necking the condition $f_B = 1$ holds (i.e., the condition $f_B < 1$ only accounts for the triaxial stress distribution that occurs after the necking formation). Therefore, as proposed in [17], a simplified approach consisting in plotting a $\sigma_{eq}-\varepsilon_{eq}$ curve with the available experimental data within the deformation range that exhibits uniaxial stress distribution (0–35 % for this material) ensures a reasonably accurate material characterization. It should be mentioned that this simple procedure to derive the hardening parameters is justified on the basis that, as reported in [18–20], such factor not only depends on the shape of the cross section of the sample (e.g., cilyndrical or rectangular) but also on the material to be tested making, therefore, its use difficult in the characterization procedure. Figure 4 shows the experimental data for the $\sigma_{eq}-\varepsilon_{eq}$ relationship together with the potential correlation $\sigma_{eq} = A^p (\varepsilon_{eq})^{n^p}$ derived from them via the application of a classical least-squares technique. The resulting hardening parameters are: $A^P = 578.27$ MPa and $n^P = 0.375$.

Lankford's coefficient

The measurement of the average Lankford's coefficient $\overline{R}$ accounting for the normal anisotropy of the sheet has been carried out according to the standard specification [21]. The expression recommended to calculate this parameter, defined as the ratio between the width and thickness deformations for sheets samples oriented at 0, 45 and 90° with respect to the direction of rolling, is $R_{0,45,90} = \ln(w/w_0)/\ln(l_0 w_0/lw)$. In this context, the average Lankford's coefficient is given by $\overline{R} = (R_0 + 2R_{45} + R_{90})/4$. The specimen dimensions were measured within the elongation range 10–25 % in order to minimize the experimental errors

Fig. 4 Tensile test: mean equivalent stress vs. equivalent deformation

Fig. 5 Multi-step deep drawing industrial application: full manufacturing sequence of ten steps
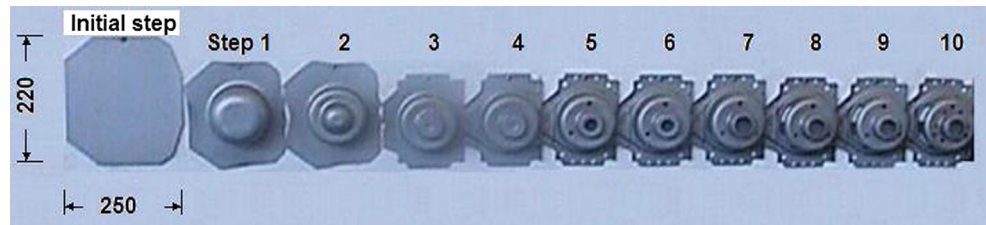
associated with the estimation of $\overline{R}$. The assumption of planar isotropy can be assessed by the so-called earing index defined as $\Delta R = (R_0 - 2R_{45} + R_{90})/4$. The Lankford's coefficients and earing index obtained for the A-G90 steel are summarized in Table 4. As can be seen, the relatively high value of $\overline{R}$ found for this steel makes it suitable for deep drawing operations. Moreover, the corresponding relatively small value of ΔR indicates that it exhibits a low planar anisotropy and, therefore, this fact justifies the use of the simplified yield criterion already presented in "Material constitutive model" section.

Damage index

The damage threshold of failure D^f is computed with the expression given in Table 1 from the equivalent stress and strains histories obtained via a numerical simulation of the tensile test (using the same numerical formulation and material properties as those detailed in "Numerical simulation of a three-step process" section) up to the instant of rupture, i.e., $\overline{e}^f = \ln(A_0/A^f) = 0.92$. The resulting value is: $D^f = 527$ MPa. As discussed in "Results and validation" and "Numerical simulation of a two-step process" sections, damage occurrence is estimated by comparing this value

with the maximum damage index developed during the different deformation stages of the forming process.

Industrial application

General description

The modeling and experimental validation of a multi-step deep drawing industrial process aimed at manufacturing a clutch lid of a commercial washing machine [22] is presented in this section. The material used for this component is the A-G90 steel. As shown in Fig. 5, the full manufacturing sequence to obtain the final product consists of ten steps which can be divided into two different stages: the first one corresponding to steps 1, 2 and 3 where the greatest sheet deformations take place, and the second stage encompassing steps 4 to 10 in which a small drawing and a bending at the base together with a series of holes and inner cuts are performed. The multi-step press automatically selects the necessary tools for each step during the whole sequence.

The complex geometry of the finished part can clearly be appreciated in Fig. 6 where the need of using a multi-step operation is apparent in this case. The initial

Fig. 6 Multi-step deep drawing industrial application: **a** initial geometry of the sheet (with a regular 10 mm × 10 mm checkered grid drawn on its surface) and **b** final product
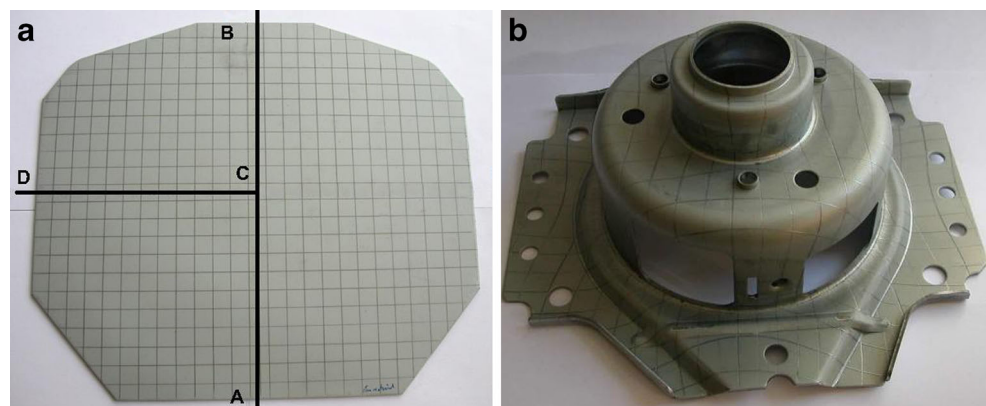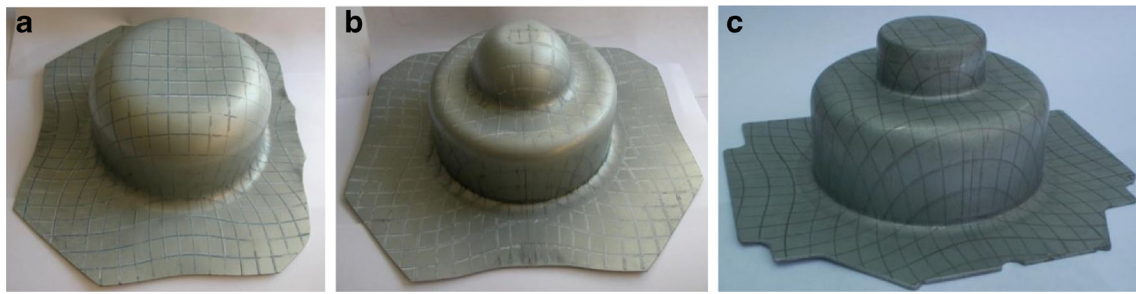
Fig. 7 Multi-step deep drawing industrial application: experimental geometric configurations at the end of the **a** first, **b** second and **c** third steps studied in this work

geometry of the sheet, which fits within a rectangle of 250 mm×220 mm, is 1.5 mm thick. A regular 10 mm× 10 mm checkered grid is drawn on its surface in order to track the in-plane sheet deformation pattern along the drawing process.

The present study focuses on the analysis of steps 1 to 3 of the full manufacturing sequence (i.e., the first stage mentioned above) because the deep drawings induced in these steps are the most critical in terms of failure occurrence. Steps 4 to 10 involve stamping, folding and cutting. Although stamping and folding could be simulated with the present model, this analysis was not carried out since these secondary forming stages were experimentally observed to not produce failure in the part. On the other hand, the simulation of cutting is not possible with the current model since a damage criterion coupled with an element removal technique should be implemented to this end.

The experimental geometric configurations at the end of the first, second and third drawing steps specifically studied here are shown in Fig. 7. The first step consists of the following operations: the lubricated steel sheet (blank) is placed on the blankholder, the die goes down and tightens the sheet against the blankholder, the punch

moves up until the desired form is achieved and, finally, the toolkit is stopped and withdrawn. A similar procedure is repeated for the second and third steps. Figure 7 clearly shows the large amount of deformation that occurs during the different forming steps. In particular, different deformation patterns can be appreciated at the end of the first step: slight biaxial extension at the bottom zone of the primary cup and high stretching at the sheet wall. The punch action for the second and third steps is mainly devoted to the forming of the secondary cup where the associated grid deformation is very similar to that obtained for the primary cup at the end of the first step.

Numerical simulation of a three-step process

The simulation of the mechanical response of the steel sheet during the first three drawing steps is carried out via a specific numerical explicit formulation defined in the context of the finite element method in which the sheet is discretized to this end using a simple thin (Kirchhoff-Love) shell three-noded triangle with only translational degrees of freedom (further details can be found in [8–10]). This element is able to deal with nonlinear kinematics (i.e., large strains and/or displacements) while the material behaviour is assumed to be governed by the hyperelastic constitutive model described in "Material constitutive model" section. The sheet material parameters used in the simulation of this multi-step process are those obtained from the A-G90 steel characterization detailed in "Material characterization" section; they are summarized in Table 5.

The finite element mesh used for the simulation of the first step of the process together with the punch and die dimensions are both depicted in Fig. 8. Due to symmetry, only one half of the geometric model is considered. As already mentioned, the blank is discretized with nearly 14000 triangular shell elements while the different tools are only meshed with surface elements on their contours

Table 5 Material properties of A-G90 galvanized steel used in the simulation of the multi-step deep drawing industrial application

Young's modulus (GPa)	147.36
Poisson's ratio	0.32
Yield strength σ_y (MPa)	167.84
Hardening coefficient A^p (MPa)	578.27
Hardening exponent n^p	0.375
Average Lankford's coefficient $\overline{R}$	1.86
Density (kg/m^3)	7850
Damage threshold of failure (MPa) D^f	527

Fig. 8 Multi-step deep drawing industrial application: **a** finite element mesh used for the simulation of the first step and **b** punch and die dimensions (in mm)
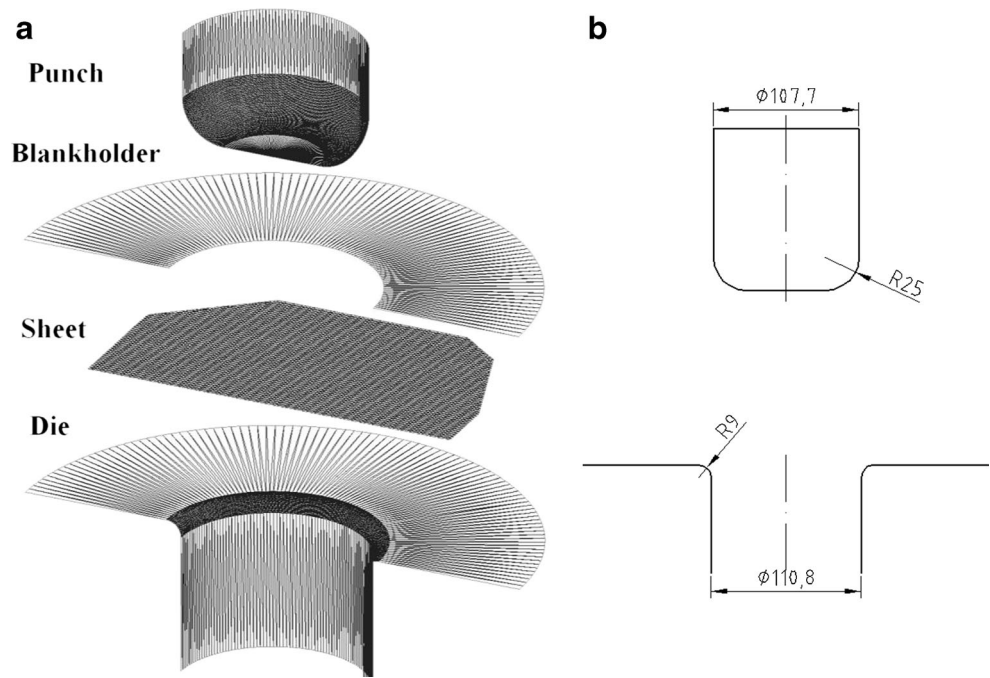

Fig. 9 Multi-step deep drawing industrial application: **a** finite element mesh used for the simulation of the second step and **b** punch and die dimensions (in mm)
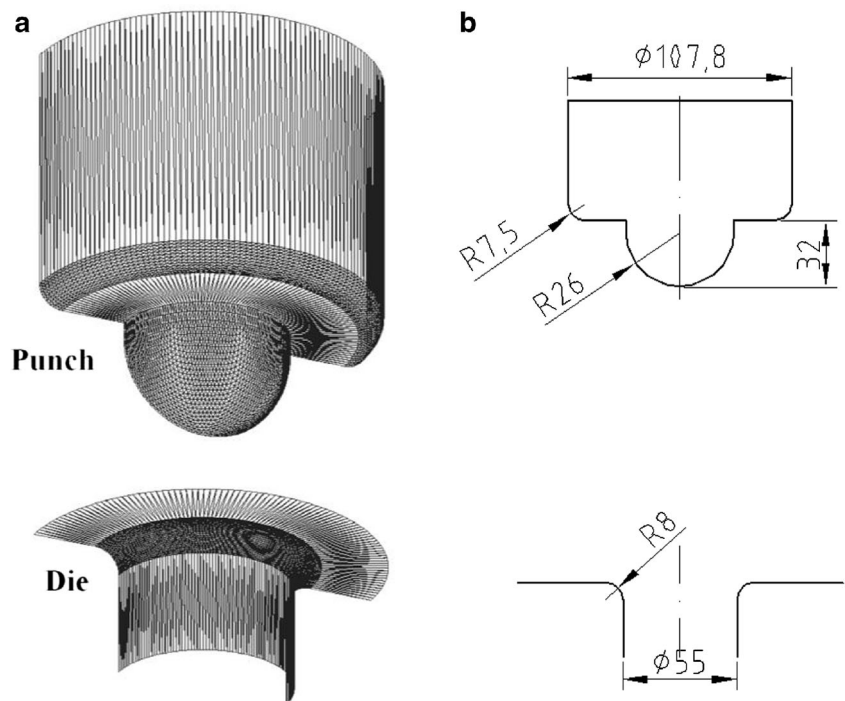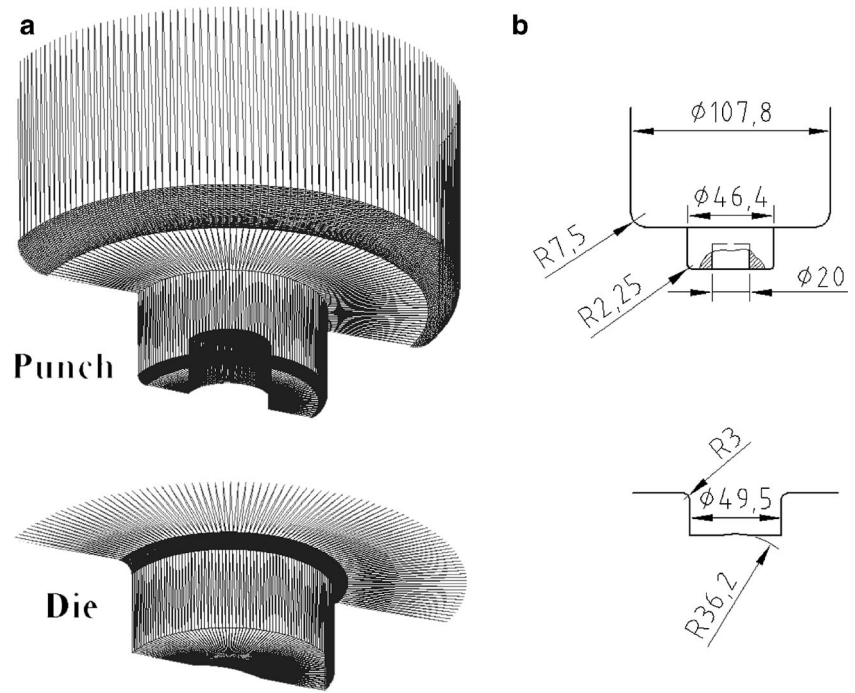
Fig. 10 Multi-step deep drawing industrial application: **a** finite element mesh used for the simulation of the third step and **b** punch and die dimensions (in mm)
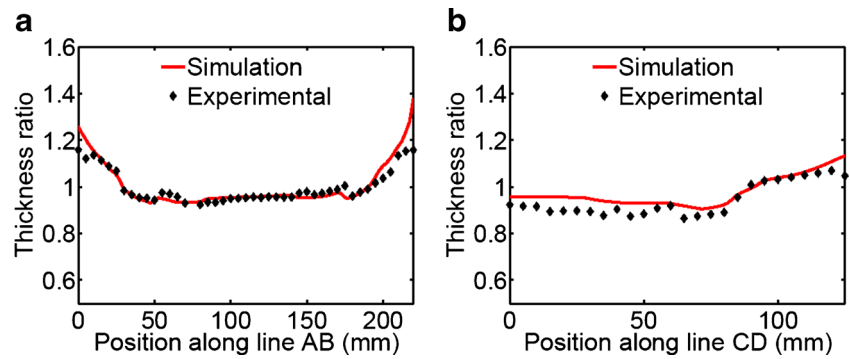

Fig. 11 Multi-step deep drawing industrial application: **a** experimental and **b** simulated sheet final geometric configuration at the end of the first step
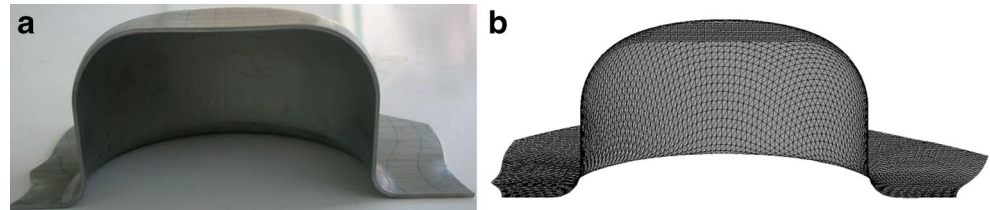
Fig. 12 Multi-step deep drawing industrial application: average experimental and computed thickness ratio profiles along **a** line AB and **b** line CD (see Fig. 6a) at the end of the first step

Fig. 13 Multi-step deep drawing industrial application: **a** experimental and **b** simulated sheet final geometric configuration at the end of the second step
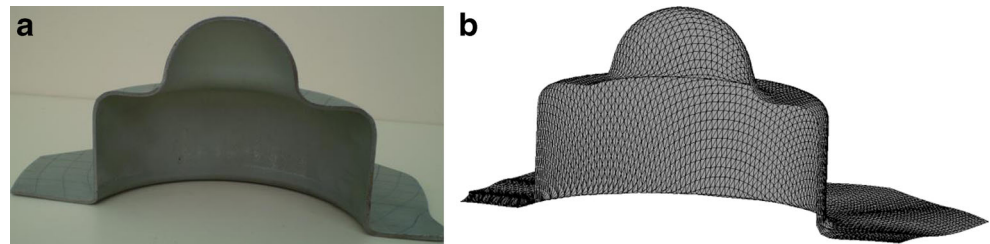
since they are assumed to be rigid. The punch and die finite element meshes corresponding to the second and third steps are respectively depicted in Figs. 9 and 10. For these two steps, the initial geometry of the sheet corresponds to that attained at the end of the previous step. Similarly, the initial stress and strain distributions are assumed to be those computed in the precedent analyses. Moreover, the same blankholder is employed in the three steps. It should be noted that all these meshes were selected on the basis that they provided nearly the same results as those obtained with finer discretizations.

The mechanical interactions between the sheet and the different tools are described via a penalty-based contact model in which the friction effects are assumed to be governed by the Coulomb law. A constant friction coefficient of 0.14 is used throughout the analysis since the same lubrication conditions were considered at every contact surface during the three forming steps where, in addition, a constant blankholder force of 17.8 kN is assumed.

It is worth noting that the low strain rate conditions under which the material parameters have been obtained (see "Material characterization" section) were also experimentally fulfilled in the three forming steps studied here where a constant punch speed of 0.1 m/s was adopted. Moreover, the numerical integration of the constitutive law along the thickness of the sheet is performed in five layers.

The pseudo static solution was computed without mass-scaling and a maximum punch velocity of 2.1 m/s. The computational cost of the analysis is 2 h on a PC with a processor i7-4790 under Windows 7 OS. This time is quite low compared with the time necessary to prepare the data and analyze the results.

Finally, no significant springback was experimentally observed (the strength-to-modulus ratio is relatively low for this material) and, hence, this effect is not considered in the simulations.

Results and validation

The experimental and numerical results obtained at the end of each drawing step encompass both the sheet final geometric configuration and the thickness ratio profiles along two representative lines (see Fig. 6a). The experimental plotted values correspond to the average of three measurements whose maximum standard deviations are 0.01 and 0.03 mm for lines AB and CD, respectively. They are separately presented, discussed and validated below.

The results corresponding to the first drawing step are shown in Figs. 11 and 12. A qualitative good agreement between the experimental and simulated final configuration of the part can be appreciated in Fig. 11. The computed thickness ratio profiles plotted in Fig. 12 also exhibit an overall reasonable fitting with the respective

Fig. 14 Multi-step deep drawing industrial application: average experimental and computed thickness ratio profiles along **a** line AB and **b** line CD (see Fig. 6a) at the end of the second step
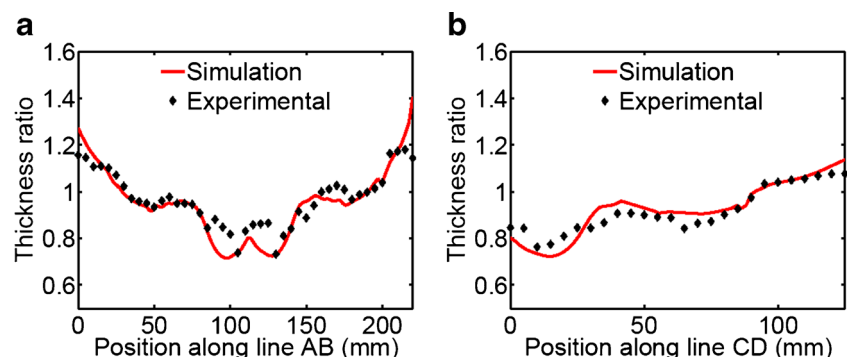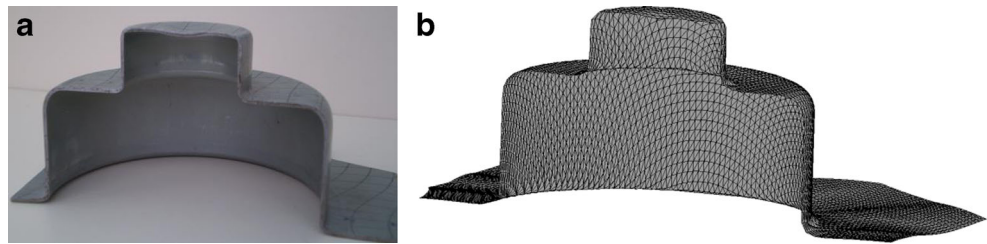
Fig. 15 Multi-step deep drawing industrial application: **a** experimental and **b** simulated sheet final geometric configuration at the end of the third step

experimental measurements. Two different sheet responses can be identified in these curves. First, a thinning occurs at the central region of the sheet where the primary cup forms. Due to the cylindrical symmetry of the punch, a nearly uniform thickness reduction is mostly found along both lines. However, a more pronounced thickness deformation can be observed in a small part of line CD owing to the initial geometry of the sheet. Second, as a result of the hoop compressive straining experienced by the material as it flows between the blankholder and die, the thickness appreciably increases on the periphery of the sheet. This zone, which remains practically clamped during the whole forming sequence, is eliminated by cutting in one of the steps of the second stage of the multi-step process. Overall, this first step induces a small biaxial stretching at the bottom of the primary cup in addition with a large contraction at the periphery of the sheet in contact with the blankholder and die. This last deformation remains constant during the full drawing sequence.

Figures 13 and 14 show experimental and computed results at the end of the second drawing step. Once again, the numerical predictions compare well with the experimental measurements. In particular, a further thickness reduction is found to take place in the vicinity of the secondary cup while the rest of the blank does not exhibit significant changes.

The experimental and predicted results attained at the end of the third step are presented in Figs. 15 and 16. It is seen that the simulation adequately describes the final shape of the

secondary cup. Moreover, the thickness reduction profiles follow the same trend as that observed for the second step, i.e. the deformation is mainly localized in a narrow region where the blank contacts the curved zones of the punch. As in the previous steps, a reasonably good experimental-numerical correlation is achieved. In summary, for the second and third steps, an increase of deformation exhibiting a nearly axisymmetric pattern develops in the region where the secondary cup is formed.

It is seen that the thickness in the central part of line AB at the end of the second and third steps is difficult to measure due to the curved geometry caused by deformation in this zone. Therefore, the associate errors in these measurements are higher than those corresponding to flat surfaces.

The thickness profiles previously shown in Figs. 12, 14 and 16 confirm the experimental observation that no severe necking is developed in the blank during the whole drawing. This fact is also ratified by the computed damage index profiles at the end of each drawing step along line AB depicted in Fig. 17a–c. Although, as expected, the damage values increase at the subsequent deformation stages, the maximum damage value is lower than the threshold of failure, i.e., a sound part is finally attained.

Numerical simulation of a two-step process

Finally, the possibility to carry out a reduced two-step drawing process, obtained by merging the second and third steps of the three-step process, is analyzed. To this end, the damage index

Fig. 16 Multi-step deep drawing industrial application: average experimental and computed thickness ratio profiles along **a** line AB and **b** line CD (see Fig. 6a) at the end of the third step
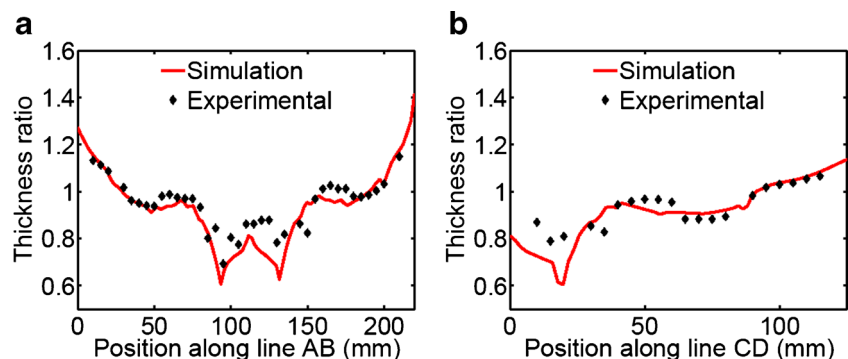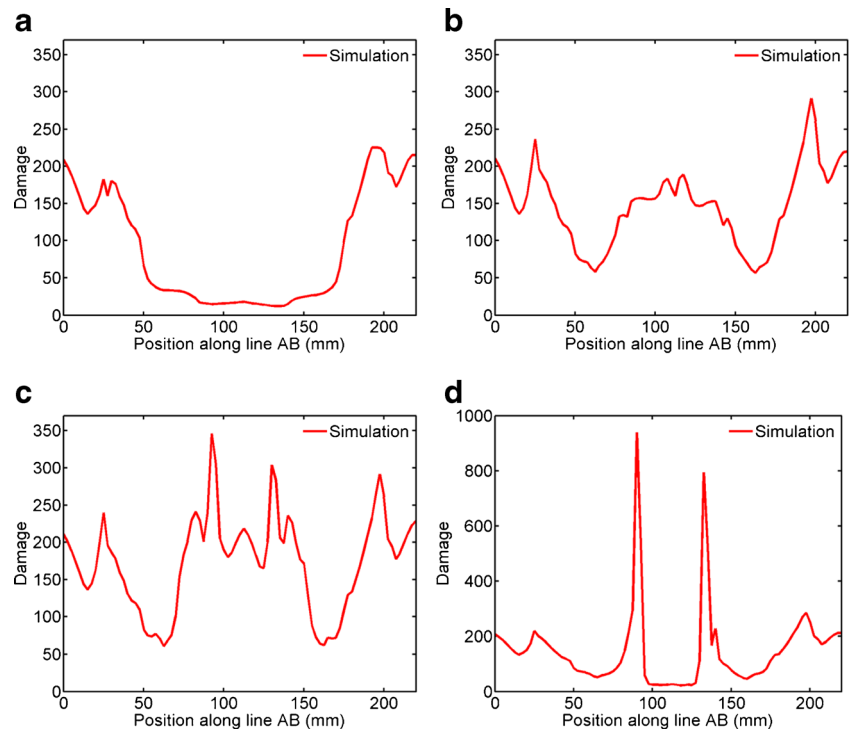
Fig. 17 Multi-step deep drawing industrial application: numerical damage profiles along line AB for **a** step 1 for the two-step and three-step processes, **b** step 2 for the three-step process, **c** step 3 for the three-step process and **d** step 2 for the two-step process

profile along line AB at the end of the forming process is computed and plotted in Fig. 17d. In this case, it is seen that the damage criterion predicts excessively large values (i.e., $D > D^f$) in specific zones of the sheet (at the zone in contact with the perimeter of punch) and, thus, this is a clear indication that the proposed step reduction is precluded.

Conclusions

The simulation and experimental validation of an industrial steel multi-step deep drawing process has been presented. In particular, this study focused on the main three drawing steps of this application. To this end, an exhaustive material characterization procedure has to be firstly conducted in order to derive the elastic and plastic parameters involved in a specific constitutive model adopted to describe the blank response during its deformation. These data have been considered in the integrated finite element analysis that has been subsequently carried out to simulate the three-step forming sequence of the present industrial process. Overall, a satisfactory experimental validation of the numerical results was achieved. Moreover, damage occurrence was predicted in a reduced two-step forming operation. In summary, the good performance of this modeling has proven that this powerful tool may be used to attain a more optimal and controlled design aimed at reducing the usually expensive trial-and-error procedures.

Limitations of the proposed methodology to be tackled in future research include: modeling the planar anisotropy, use of non-associate plasticity, consideration of texture evolution via a polycrystalline plasticity approach and assessment of the shell plane stress assumption of the shell element by comparing its response with that provided by solid finite elements.

References

1. Dixit US, Joshi RN, Dabim JM (2011) Incorporation of material behavior in modeling of metal forming and machining processes: a review. Mater Des 32:3655–3670
2. Hill R (1948) A theory of the yielding and plastic flow of anisotropic metals. Proc R Soc Lond A193:281–297
3. Salehinia I, Shahani AR (2009) Effect of sheet anisotropy on the wear in deep-drawing process of a cylindrical cup. Int J Mech Sci 51:856–868
4. García C, Celentano D, Flores F, Ponthot JP, Oliva O (2006) Numerical modelling and experimental validation of steel deep drawing processes Part II. Applications. J Mater Process Technol 172:461–471
5. Elgueta M (2002) Ductile damage analysis of sheet metal forming. J Mater Process Technol 121:148–156
6. Lou Y, Huh H (2013) Evaluation of ductile fracture criteria in a general three-dimensional stress state considering the stress triaxiality and the Lode parameter. Acta Mech Solida Sin 26(6):642–658

7. Yu Y, Haibo W, Min W (2011) Prediction of fracture in press bend forming of aluminum alloy high-stiffener integral panels. Comput Mater Sci 50:2232–2244

8. Flores F, Oñate E (2001) A basic thin Sheet triangle with only translational DOFs for large strain plasticity. Int J Numer Methods Eng 51:57–83

9. Flores F (2000) Un algoritmo de contacto para el análisis explícito de procesos de embutición. Revista Internacional de Métodos Numéricos para Cálculo y Diseño en Ingeniería 16:421–432 **(in Spanish)**

10. (2014) STAMPACK: a general finite element system for sheet stamping forming problems. www.quantech.es. Accessed 2014

11. Clift SE, Hartley P, Sturgess CEN, Rowe GW (1990) Fracture prediction in plastic deformation processes. Int J Mech Sci 32:1–17

12. DIN 1623 Specification (1987) Cold reduced sheet and strip technical delivery conditions, mild unalloyed steels for vitreous annealing. Deutsche Norm, Deutsches Institut für Normung

13. ASTM E8-88 Specification (1988) Standard test methods for tension testing of metallic materials. Annual Book of ASTM Standards, American Society for Testing and Materials

14. DIN 50145 Specification (1988) Testing of metallic materials. Deutsche Norm, Deutsches Institut für Normung

15. ASTM E646-00 Specification (2000) Standard test method for tensile strain hardening exponents (n-values) of metallic sheet materials. Annual Book of ASTM Standards, American Society for Testing and Materials

16. Bridgman P (1952) Studies in large plastic and fracture. McGraw-Hill Book Company, London

17. García C, Celentano D, Flores F, Ponthot JP (2006) Numerical modelling and experimental validation of steel deep drawing processes Part I. Material characterization. J Mater Process Technol 172:451–460

18. Cabezas E, Celentano D (2004) Experimental and numerical analysis of the tensile test using sheet specimens. Finite Elem Anal Des 40(5–6):555–575

19. Celentano D, Cabezas E, García C, Monsalve A (2004) Characterization of the mechanical behaviour of materials in the tensile test: experiments and simulation. Model Simul Mater Sci Eng 12:425–444

20. Celentano D, Cabezas E, García C (2005) Analysis of the Bridgman procedure to characterize the mechanical behavior of materials in the tensile test: experiments and simulation. ASME J Appl Mech 72(1):149–152

21. ASTM E517-87 Specification (1988) Plastic strain ratio R for sheet metal. Annual Book of ASTM Standards, American Society for Testing and Materials

22. CTI, (2014). www.cti.cl. Accessed 2014